Renewable Energy 216 (2023) 119084

Contents lists available at ScienceDirect

Renewable Energy

journal homepage: www.elsevier.com/locate/renene

Planning the installation of building-integrated photovoltaic shading devices: A GIS-based spatiotemporal analysis and optimization approach

Yuxuan Ye [a,c,d], Rui Zhu [b,*], Jinyue Yan [e], Lin Lu [e], Man Sing Wong [f], Wei Luo [g,h], Min Chen [i,j,k], Fan Zhang [l], Linlin You [m], Yafei Wang [a,c], Zheng Qin [b]

[a] Key Laboratory of Regional Sustainable Development Modeling, Institute of Geographic Sciences and Natural Resources Research, Chinese Academy of Sciences, Beijing, 100101, China
[b] Institute of High Performance Computing (IHPC), Agency for Science, Technology and Research (A*STAR), Singapore, 138632, Republic of Singapore
[c] Country College of Resources and Environment, University of Chinese Academy of Sciences, Beijing, 100190, China
[d] School of Geography, Nanjing Normal University, Nanjing, 210023, China
[e] Department of Building Environment and Energy Engineering, The Hong Kong Polytechnic University, Kowloon, Hong Kong, China
[f] Department of Land Surveying and Geo-Informatics, The Hong Kong Polytechnic University, Kowloon, Hong Kong, China
[g] Geography Department, National University of Singapore, 117570, Singapore
[h] Saw Swee Hock School of Public Health, National University of Singapore, 117549, Singapore
[i] Key Laboratory of Virtual Geographic Environment (Ministry of Education of PR China), Nanjing Normal University, Nanjing, 210023, China
[j] State Key Laboratory Cultivation Base of Geographical Environment Evolution, Nanjing, 210023, China
[k] Jiangsu Center for Collaborative Innovation in Geographical Information Resource Development and Application, Nanjing, 210023, China
[l] Department of Civil and Environmental Engineering, The Hong Kong University of Science and Technology, Kowloon, Hong Kong, China
[m] School of Intelligent Systems Engineering, Sun Yat-Sen University, Shenzhen, 518107, China

ARTICLE INFO

Keywords:
Building-integrated photovoltaics (BIPV)
Photovoltaic-integrated shading device (PVSD)
Solar PV planning
Geographical information system
Multi-objective optimization

ABSTRACT

Building-integrated photovoltaics (BIPV) can produce power while occupying little urban space. Photovoltaic-integrated shading devices (PVSDs) are a key component of BIPV that can generate electricity while blocking excess daylight. However, previous studies have lacked a systematic design of PVSDs that accurately estimates the trade-offs between indoor sunshade duration and electricity generation. This study proposes a multi-objective optimization framework for maximizing PV potential, minimizing PV area, and enabling proper sunshade duration in complex urban surfaces. A GIS-based spatiotemporal analysis and optimization approach was applied to three PVSD planning scenarios: (i) parallel to the horizontal land surface, (ii) inclined at an angle equal to the local latitude, and (iii) rotated in real-time to keep the PV surface perpendicular to the solar radiation. Different PV widths are determined under different scenarios considering power generation and solar shading duration. In the real-time rotating scenario, the optimized 0.7-m-wide PVSDs can generate 0.861 GWh of electricity annually, with a competitive average power generation efficiency of 0.811 kWh/m^2/day and a solar shading duration of 6.61 h/day. Flexible installation scenarios are suggested to account for shading from other upper PVSDs and surrounding buildings. This study can facilitate solar farming in global cities and contribute to renewable energy penetration.

1. Introduction

Global cities generated approximately 75% CO_2 emissions, causing frequent heat waves and global warming [1]. To mitigate global warming, reduce air pollution, and achieve the United Nation's Sustainable Development Goals [2,3], the global community facilitates the use of renewable energy for sustainable development [4,5]. Since solar energy is credited as a free, clean, unlimited, and eco-friendly renewable energy source [6], people have witnessed a growing interest in capturing solar energy locally to reduce its dependence on traditional electric utilities in recent years [7].

It is reasonable to install building-integrated photovoltaics (BIPV) at locations having abundant solar energy to generate a large amount of electricity without taking up precious land in cities. BIPV products can

* Corresponding author. Systems Science Department, Institute of High Performance Computing (IHPC), Agency for Science, Technology and Research (A*STAR), Singapore.
E-mail address: zhur@ihpc.a-star.edu.sg (R. Zhu).

https://doi.org/10.1016/j.renene.2023.119084
Received 21 March 2023; Received in revised form 27 June 2023; Accepted 24 July 2023
Available online 26 July 2023

be grouped into four macro-categories [8]: PV-façades [9,10], PV-roofs [11–13], PV-windows and overhead glazing [14–16], and PV-sunshades [17–20]. The evaluation of these approaches was traditionally based on simulation software packages or Computer Aided Design (CAD) models, such as EnergyPlus [21–23] and PVsyst [24–26]. For example, an early research modeled a BIPV south-orientated tilted roof at 20 different locations ranging from 0°N to 85°N latitude and demonstrated the correlation between the optimal tilt angle for a fixed BIPV system and the location of the system deployment, i.e. the latitude [27]. According to a study that assessed the technical and economic viability of using a thin-film Cadmium telluride BIPV system in six Brazilian cities, it was suggested that BIPVs integrated on rooftops and façades could meet building's annual energy consumption [28]. High-rise buildings have a high potential for installing BIPV on façades, but they may also cause significant shading on neighboring buildings throughout the year. Besides, L-shaped and U-shaped buildings are typically less efficient for BIPV deployment, primarily due to the shading from solar inter-building reflections and surrounding buildings [29]. To address the concern about BIPV's economic suitability, previous studies quantified its societal and environmental impacts and conducted economic analyses such as lifecycle cost analysis [30,31].

Photovoltaic-integrated shading devices (PVSDs), a type of BIPV product, are defined as the components of building shading devices that are substituted by or coated with PV elements in this study, especially panels, overhangs, and awnings. This technology enables to convert excessive incident solar radiation into power in situ as well as balance the thermal and lighting environment of the building [8], which has attracted more attention recently. The integration of PV with *Brise–Soleil* systems (i.e., PVSD) has been proven to be more technically efficient than other BIPV products like PV-façades and PV-roofs, and its efficiency is comparable to that of roof-mounted standalone PV systems [32,33]. According to the study [34], PVSDs that are designed and positioned at the optimal orientation and tilt can effectively prevent undesired direct sunlight and irradiation, and act against overheating and glare, while ensuring a favorable electrical yield.

So far, most PVSDs have been applied to static scenarios, especially for office buildings [35]. One study performed a PVSD simulation on a single-family detached house in Famagusta, Cyprus, and found that the strategic use of PVSDs for openings facing east, west, and south can reduce its energy consumption by about 50% in three peak months of the year [36]. It was discovered that PVSDs face to the south with a 30° tilt angle could maximize the electricity generation in a series of simulations for office space in Hong Kong [19]. A previous study has compared different scenarios among 15 cases and concluded that passive building design with shading devices is the most effective and balanced solution, which can achieve substantial potential energy savings while maximizing thermal and visual comfort [37]. Despite the achievement, the viability of assessing the potential of PVSDs in fine-scale urban areas is typically neglected, and existing studies have not yet gone beyond the building level. To bridge the gap, it is essential to develop accurate methods for estimating the solar potential distribution over larger areas, which can provide valuable insights into the placement and configuration of PVSDs in the broader context of urban environments. Furthermore, appropriate and scientific planning of PVSDs with different usage preferences is needed, which considers factors such as the tilt angle of the PV modules, as well as the energy needs of the building and the comfort level of the occupants.

Due to the spatial and temporal complexity of real-world urban environments, expanding the solar PV simulation to the three-dimensional (3D) urban scale is a key challenge. Geographic information system (GIS) techniques have been explored to address the fine-scale PV planning challenges. The web-based PV estimation platform PVGIS was designed to evaluate large-scale PV potential in the early years [38,39]. Afterward, a combined vector-voxel approach was used to calculate solar radiation in 3D city models [40]. An algorithm called SOL was developed to calculate global solar irradiance for a set of points located on urban surfaces using Light Detection And Ranging (LiDAR) data with solar astronomical models [41]. One research went a step further to incorporate the 3D City Geography Markup Language (CityGML) model into the SOL algorism [42]. An integration of CAD-related 3D solutions and GIS-related regional solutions is introduced to fulfill the requirements of multiscale solar potential evaluation [43]. These approaches fully utilize the GIS's large-scale spatial analysis capabilities, but limited thought has been given to integrating BIPV modeling with GIS technology in urban structures, especially building façades.

One state-of-the-art methodology developed the 3D intersection method in PostgreSQL to model the solar capacity of a city as 3D point clouds (i.e. a discrete set of 3D points in space) covering the whole urban surface [44,45], which takes real-world atmospheric conditions and shadow effect made by nearby buildings into account and allows fast computation of large amounts of buildings. This physically sound model has been applied to investigating urban PV planning issues, such as estimating solar PV potential on urban noise barriers [46], charging shared electric scooters [47], and typical urban architecture [48]. Overall, these previous studies have generated valuable scientific insights into understanding the solar PV potential of cities.

However, a perspective that considers the heterogeneity of local-scale spatial and temporal PV potential in the planning of PVSDs is currently lacking. Evaluating the solar PV potential of PVSDs in urban areas is crucial for designing and implementing sustainable building policies. Ideally, such an evaluation should be performed in a multi-objective optimization framework, balancing competing building performance factors influenced by PVSDs, over a large geographical extent to reveal urban solar potential distribution characteristics under intricate shading events, and considering a high temporal resolution to understand the dynamic variation of solar irradiation and match real power demands. This has rarely been accomplished in previous studies. Therefore, our study aims to implement this evaluation and precisely demonstrate the spatiotemporal PV potential distribution of PVSDs in an urban area. In this way, we can answer questions of "where to build", "when to profit", and "how to improve".

In this study, we have collected cloud cover data and three-dimensional building footprint data to estimate the solar PV potential of PVSDs on the extracted windows in the study area, demonstrating the huge potential of local renewable energy systems. The novelties of this study are elaborated as follows: (i) proposing a multi-objective optimization approach to maximize distributed solar farming (i.e., achieve the highest possible deployment and utilization of solar energy through distributed PV systems) and effective shading duration (which considers the varying shading requirements in different seasons) on the PVSDs; (ii) analyzing and comparing three PVSD deployment scenarios to determine optimal modeling parameters, and discussing the differences in their energy and shading performances; and (iii) revealing the spatiotemporal solar PV heterogeneity of PVSDs in an urban environment to guide the strategic placement. Our findings can promote energy transition in urban areas and contribute to the realization of the nearly zero energy buildings (nZEB) concept.

The rest paper is structured as follows. Section 2 proposes the methodology to perform multi-objective optimization for PVSD installation. Section 3 introduces the case study to empirically evaluate the developed methodology. Section 4 presents the modeling results and investigated the differences between different scenarios. Section 5 presents the discussion and Section 6 draws the conclusion.

2. Methodology

This study proposed a multi-objective optimization framework for PVSD planning, balancing the trade-off between maximizing solar farming and providing proper sunshade duration. The framework contains three major stages (Fig. 1): first, accurately modeling spatiotemporal distribution of solar potential on 3D urban surfaces throughout the year based on the statistically significant weather data and building

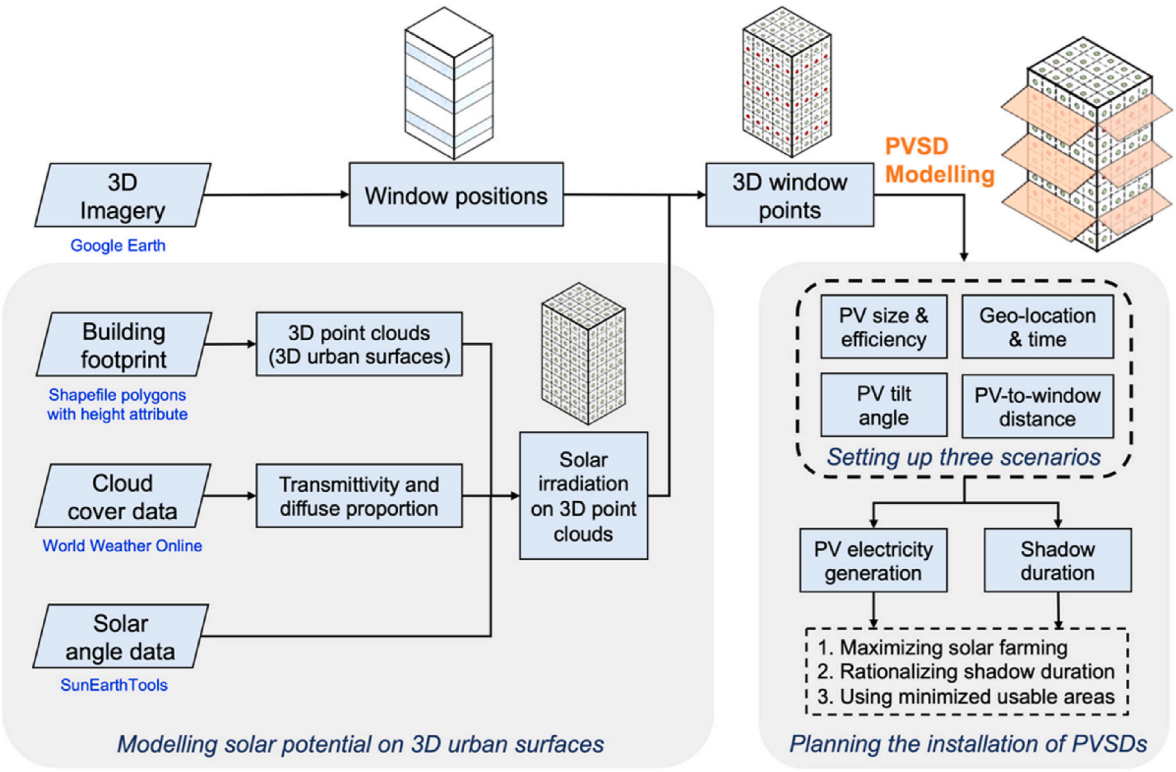

Fig. 1. A flowchart of modeling the PVSDs.

footprint data enriched with the height attribute; second, extracting the window areas from street-view images and estimating the solar PV potential on the PVSD surfaces based on the three proposed scenarios; third, planning the optimal installation locations for PVSDs by considering the merits of each scenario. The abbreviations used in this study are listed in Table 1.

2.1. Computation of land surface solar irradiation

To accurately assess the potential of solar irradiation on land surfaces, it is crucial to account for the impact of cloud cover under various weather conditions. This study calculated the monthly average atmospheric transmittivity and diffuse proportion based on cloud cover data according to a straightforward yet effective method [49]. Transmittivity (T) represents the amount of light passing through a material, such as a window or solar panel, while diffuse proportion (D) measures of how much of the light is scattered or diffused rather than traveling in a straight line. By incorporating T and D, we can calculate the direct and diffuse solar irradiation on land surface, which will be used to determine the real-world spatiotemporal solar potential. The formulae are presented in Equations (1) and (2):

$$T = 0.7 \times P_{clear} + 0.5 \times P_{partial-cloudy} + 0.3 \times P_{cloudy} \# \quad (1)$$

$$D = 0.2 \times P_{clear} + 0.45 \times P_{partial-cloudy} + 0.7 \times P_{cloudy} \# \quad (2)$$

where T is the fortnightly average atmospheric transmittivity, D is the fortnightly average diffuse proportion, P_{clear} is the percentage of clear days per two weeks, $P_{partial-cloudy}$ is the percentage of partly cloudy days and P_{cloudy} is the percentage of cloudy days.

2.2. Estimation of spatiotemporal solar distribution on 3D urban surfaces

This study utilizes a well-established model to estimate solar distribution on 3D urban surfaces [44], which has been suggested to be accurate and reliable in many studies [45–48,50]. In the model, urban surfaces (i.e., rooftops, façades, and ground) are represented by 3D point clouds, where each point records the quantified solar irradiations on a unit area. The urban surfaces are denoted by $\mathscr{G}$ and consist of building footprints associated with the height attribute, which can be decomposed into rooftops, façades, and ground. Each element $g \in \mathscr{G}$ is discretized into a set of homogeneous grids with a constant resolution that are spatially contiguous with each other. Centroids denoted by $\mathscr{P}$ are extracted from the grids to present 3D point clouds of the urban surfaces. Each point $p \in \mathscr{P}$ is represented by a unique ID, a 3D coordinate, and a building index number. After that, a full set of parallel solar radiation vectors passing through the atmosphere and arriving at the point clouds $\mathscr{P}$ are determined and denoted by $\mathscr{R} = \{r\}$.

A solar radiation vector r can be expressed as a tuple $\langle e, \beta, t, l, u_0 \rangle$, which means that r comes from the atmosphere at an elevation e and an azimuth β with qualified irradiation u_0 and arrives on an urban surface located at a 3D coordinate l at time t. The 3D intersection between urban surfaces $\mathscr{G}$ and radiations $\mathscr{R}$ is furthermore carried out to produce a set of 3D shadow surfaces denoted by $\mathscr{S}$. Several modifications have been made and recorded by $\mathscr{S}'$ to make the initial shadows $\mathscr{S}$ physically correct, including removing solar-facing or low-rise coincident facades and reshaping shadow surfaces by nearby buildings and concave rooftops. Finally, for each point $p \in \mathscr{P}$, the solar irradiation u is set to 0 if it is below the shadow surface $\mathscr{S}'$, else u is expressed as $f(u_0)$.

2.3. Estimation of the power potential of the PVSD

The estimation of the power potential of the PVSD is made by physical modeling, consisting of an accurate estimation of shadow distribution and solar potential redistribution on PVSDs. It shows that the sunlight is obstructed by the PVSDs that are installed perpendicularly to the wall, creating a grey shadow area on the blue window (Fig. 2a). The width and length of the PVSDs are denoted by w and l, respectively. The distance from the top of the window to the PVSD is represented by d, and the height of the window is h. The interval between two adjacent PVSDs is indicated by ι, the angle between the PVSD and the wall by θ, the solar

Table 1
Abbreviations used in this study.

No.	Abbre.	Nomenclature
1	T	Transmittivity
2	D	Diffuse proportion
3	P_{clear}	The percentage of clear days per two weeks
4	$P_{partial-cloudy}$	The percentage of partly clear days per two weeks
5	P_{cloudy}	The percentage of cloudy days per two weeks
6	$\mathscr{G}$	Urban surfaces
7	g	Element of urban surface (i.e. building)
8	$\mathscr{P}$	A set of all the point clouds
9	p	A point
10	$\mathscr{R}$	A set of all the solar radiation vectors
11	r	A solar radiation vector
12	e	Solar elevation angle
13	β	Solar azimuth angle
14	t	Instant of time
15	l	Location
16	u_0	Qualified solar irradiation of a solar vector
17	u	solar irradiation of a point
18	$\mathscr{S}$	A set of 3D shadow surfaces
19	$\mathscr{S}'$	A set of the modified 3D shadow surfaces
20	w	Width of the PVSD
21	l	Length of the PVSD
22	d	Distance from top of window to PVSD
23	h	Height of the window
24	ν	Interval between two adjacent PVSDs
25	θ	Tilt angle of the PVSD
26	H_s	Height of the shadow on the façade made by PVSD
27	A	Area of the PVSD
28	A'	Shadowed area of the PVSD
29	α	Azimuth of footprint polyline
30	γ	The absolute difference between α and β
31	u'	Solar irradiation on the PVSD
32	E_y	Annual electricity generation of the PVSD
33	$\widetilde{E}_y$	Annual electricity generation of the PVSD per square meter
34	$\widetilde{E}_d$	Electricity generation of the PVSD per square meter per day
35	TH	Threshold
36	τ	Effective sunshade duration
37	F	The objective function
38	$\mathscr{W}$	A set of extracted 3D window points
39	w	A 3D window point

elevation angle by e, and the height of the shadow on the façade made by the PVSD by H_s. The estimation considers three different situations: (i) $H_s < h$, part of the window is shadowed, (ii) $h < H_s < \nu$, the entire window is shadowed, and other PVSDs below will not be affected, and (iii) $H_s > \nu$, the shadow created by PVSDs can cover the entire window and partially or fully cover the PVSDs or windows below, which is considered as *overshadow*.

Fig. 2b draws the side view of the model, where the upper inclined PVSD with an area of A creates full shading for the window and simultaneously blocks part of the lower PVSD with a shadowed area of A'. The shadowed area A' is computed in Equation (3). Considering the difference between the solar irradiation azimuth and the façade azimuth, the height of shadow H_s is calculated in Equation (4). Fig. 2c depicts a top view of the model, where the clockwise arrows make up an exterior ring of the building footprint. The azimuth of each footprint polyline is denoted by α, the solar azimuth is represented by β, and the absolute difference between α and β is denoted by γ. On this basis, solar irradiation on the PVSD is expressed as u' and calculated in Equation (5).

$$A' = \frac{(H_s - \nu) \bullet sin(90 - e) \bullet l}{sin(90 + e - \theta)} \# \tag{3}$$

$$H_s = \frac{w \cdot sin\,\theta}{sin(\alpha - \beta)} tan\, e + w \cdot cos\,\theta \# \tag{4}$$

$$u' = u \bullet \frac{\cos(\theta - e)}{\cos(e)} \bullet (w \bullet l - A') \# \tag{5}$$

2.4. Scenario-based priority optimizations

Since several PVSD usage preferences may result in significantly different optimization results, this study refines three preferences corresponding to different priorities to facilitate the optimizations: (i) sight view first with PVSD horizontally installed, (ii) shading and sight view compatible with PVSD inclinedly installed, and (iii) electricity generation first with PVSD always perpendicular to the varying solar irradiation. They are more formally represented by: (i) static horizontal scenario (SHS), where all PVSDs are installed parallel to the horizontal ground, which is the most common solution (Fig. 3a); (ii) static inclined scenario (SIS), where all PVSDs are tilted at an angle equal to the latitude of the location, which allows for maximum electricity output by facing approximately between the sunlight's highest and lowest points in summer and winter (Fig. 3b); (iii) real-time rotation scenario (ROS), where the angle of all PVSDs varies in real-time to match the current solar elevation angle (Fig. 3c). In Fig. 1, the shaded area is represented in grey, the window is indicated in blue, and the area where 3D solar vectors arrive on the PVSD is presented in orange. The yellow circle represents the sun.

2.5. Multi-objective optimizations

PVSDs can serve multiple purposes such as electricity generation, indoor cooling, and architectural aesthetics [8]. However, some of these purposes may conflict with each other when it comes to PVSD planning.

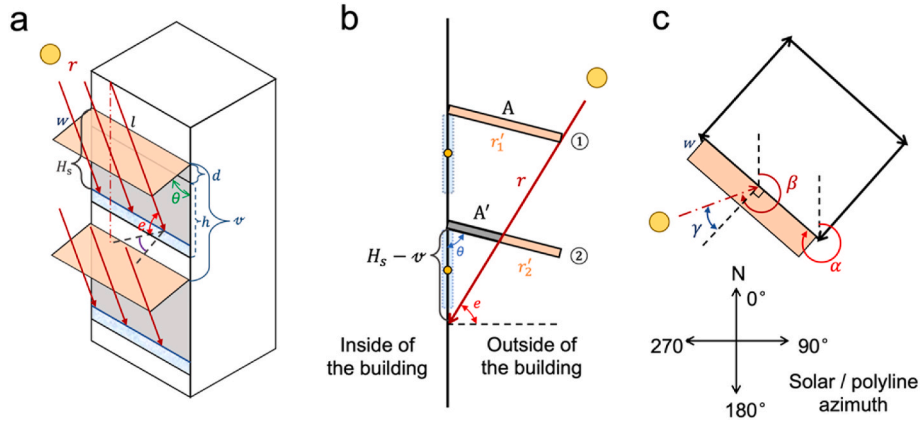

Fig. 2. The PVSD power generation calculation model in 3D view. (a) Solar irradiation is obscured by PVSDs and generates shadows on the window surface. (b) A side view showing that solar irradiation causes *overshadow* on the lower PVSD. (c) A top-down view showing the relationship between solar azimuth and building polyline azimuth.

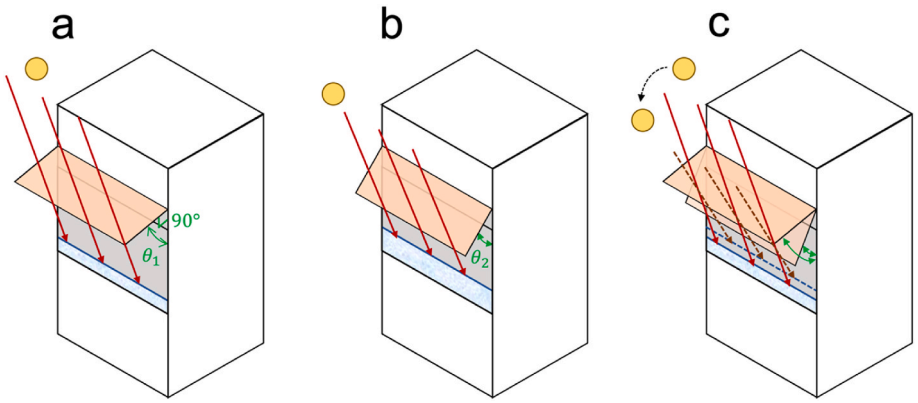

Fig. 3. Three scenarios for installing PVSD on building facades. (a) The static horizontal scenario. (b) The static inclined scenario. (c) The real-time rotating scenario.

For example, maximizing solar farming with an optimal tilt angle may result in insufficient indoor daylighting, causing an increased energy consumption for artificial lighting. Therefore, it is important to consider the trade-offs to optimize the PVSD installation. That is to say, the PVSDs should not only generate electricity as much as possible, but also provide proper sunshades with sufficient daylight.

The PVSD's annual electricity generation E_y must exceed a threshold TH to guarantee an adequate amount of electricity generation in any independent PVSD planning scenario. The threshold TH is set at 60% of the maximum E_y in the specific scenario to adapt to the data range and improve the consistency of results across different scenarios, as well as to achieve a compromise between sensitivity and specificity. The adverse impact on power generation of surrounding buildings that cast shadows on PVSDs can be disregarded by setting TH. Windows that are frequently shaded by surrounding structures will inherently receive less solar radiation over a year than windows with unobstructed exposure, resulting in a lower solar PV potential. This conflict with our optimization goal of maximizing PV potential while minimizing PVSD area.

The solar shading capability is measured by effective sunshade duration τ, which represents the average number of hours during which the PVSD provides proper shading. The term "proper shading" refers to providing the right amount of shading at the right time. Thus, the metric τ is designed to be time-dependent and adaptable to different seasons. It draws inspiration from previous relevant metrics, such as Window Sunlight Hours [51] (cumulative sunlight exposure duration of windows from 8 a.m. to 4 p.m. on January 21st) and Useful Daylight Illuminance [52] (the percentage of occupied hours when daylight levels on the horizontal working plane fall within certain ranges). In summer, PVSDs are required to block the majority of sunlight to reduce indoor heat as possible. In spring, the shading requirement for PVSDs can be slightly eased. While in winter, PVSDs should allow a moderate amount of sunlight to enter the room, providing warmth and natural light. Hence, upper and lower limits are set for winter to avoid non-sufficient and excessive sunlight. The effective sunshade duration τ is mathematically expressed in Equation (6):

$$\tau = \sum_{t=9}^{18} f(H_s, t)\# \tag{6}$$

The indicator function $f(H_s, t)$ is set to 1 when the conditions shown in Equation (7) are met; otherwise, it is set to 0.

$$\begin{cases} H_s \geq 0.8 \times h, if\ t\ in\ summer \\ 0.4 \times h \leq H_s \leq 0.7 \times h, if\ t\ in\ winter\ \# \\ H_s \geq 0.6 \times h, if\ t\ in\ spring/autumn \end{cases} \tag{7}$$

The objective functions are to minimize the total PVSD area A (Equation (8)), while simultaneously maximizing the accumulated solar irradiation u (Equation (9)) and maximizing the effective sunshade duration τ (Equation (10)). The optimization approach followed a stepwise approach. The first optimization priority is to maximize the accumulated solar irradiation, followed by the second priority of maximizing the effective sunshade duration. In each optimization scenario, if the determined PVSDs consistently meet the power generation requirements and provide proper shading throughout the year, it indicates a convergence of the optimization process. Through pre-experiments, we have determined that setting the value of d to 0 is optimal for maximizing both PV generation and the effective sunshade duration in most seasons. During each simulation iteration, the urban surfaces $\mathscr{G}$, 3D point clouds $\mathscr{P}$, solar radiation $\mathscr{R}$, and historical meteorological conditions remain unchanged, and the initial parameters, including the width w and tilt angle θ, are updated for all window points in different scenarios. The constraints of the parameters used in the optimization modeling are listed in Table 2.

$$F_A = min\left(\sum A\right)\Big|\left(E_y \geq TH\right)\# \tag{8}$$

$$F_u = max\left(\sum u\right)\Big|F_A\# \tag{9}$$

$$F_\tau = max\left(\sum \tau\right)\Big|F_u\# \tag{10}$$

3. Empirical evaluation

3.1. Study area

Hong Kong, a highly urbanized city with a population of over seven million, has a land area of barely 1114 km^2 [53]. High-rise residential and commercial buildings consume a significant amount of energy in densely populated areas. In 2019, buildings in Hong Kong consumed

Table 2
Constraints of the parameters for the modeling analysis.

Parameter	Unit	Range	Explanation
Width of the PVSD (w)	[meter]	0.5–1	The width of the PVSD is iterated from 0.5m to 1m with a step size of 0.1m.
Tilt angle of the PVSD (θ)	[degree]	0–90	The angle between the PVSD and the wall should be no more than 90 °.
Distance from top of the window to the PVSD (d)	[meter]	0–0.2	The distance from the top of the window to the PVSD should be no more than 0.2m to guarantee solar shading capacity.
Threshold to guarantee an adequate amount of electricity generation (TH)	[kWh]	0.6 • max (Ey)	The threshold is set at 60% of the maximum E_y in the specific scenario to adapt to the data range.

197,730 TJ of energy, with 158,000 TJ (79.91%) being electricity [54]. Located at 22.3N° latitude with a sub-tropical climate, Hong Kong has abundant solar energy resources, with an annual average global horizontal solar irradiance of 1.29 MWh/m^2 [55,56]. However, the high-rise and high-density nature of Hong Kong makes it challenging to develop large-scale solar facilities, and less than 0.01% of its electricity is currently produced from solar PV farming [54]. To achieve the grand goal of net-zero carbon emissions in electricity generation before 2050, the Hong Kong Government has introduced the Feed-in Tariff scheme in recent years, encouraging the community to develop distributed renewable energy. It is estimated that all approved solar energy generation systems can yield about 200 million kWh of electricity and reduce about 140, 000 tons of carbon emissions each year [57]. Therefore, there is a great opportunity to deploy distributed BIPV systems in Hong Kong. The study area is the campus of the Hong Kong Polytechnic University (Fig. 4), one of the densest urban areas containing 28 buildings in an area of 0.095 km^2.

3.2. Data collection

The building footprint data was obtained from the Lands Department of the Government of the Hong Kong Special Administrative Region in ESRI Shapefile format. The data contains various attributes, such as identification number, building height, and area. It was used to extract building outlines and building pixels to calculate the solar potential of each building. The cloud cover percentage data in 2018 was obtained from World Weather Online [58], which was used to calculate T and D that conclusively determine land surface solar irradiation. Since the study area is relatively flat, the effects of terrain variation on solar irradiation distribution were not considered. Besides, we assume that all rooftops in the study are flat, since sloped rooftops have an insignificant impact on the distribution of solar energy on façades.

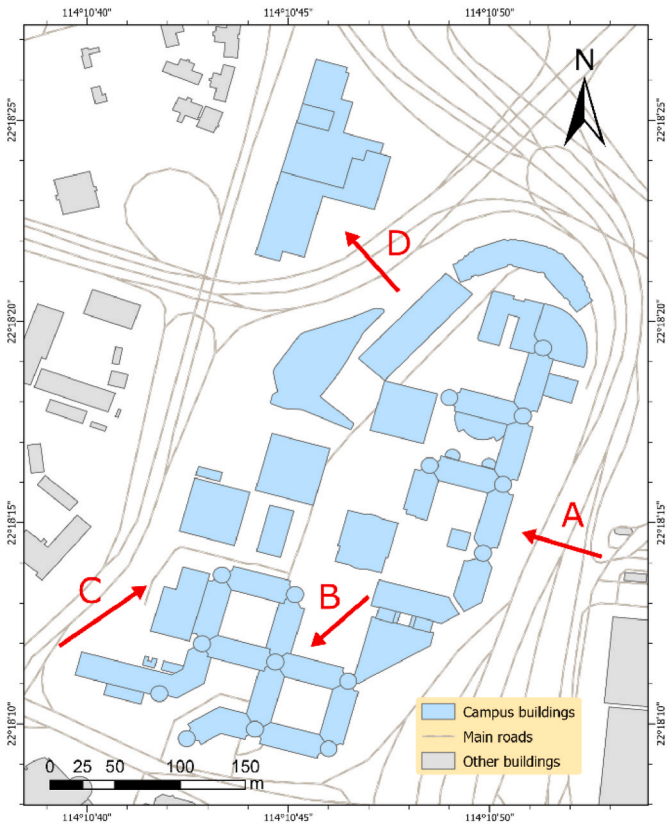

Fig. 4. The overview map of the study area. The red arrows indicate the viewing orientation of the study area examples shown in Fig. 10.

3.3. Data pre-processing

For easy computation and statistics, this study defined the constructed 3D point clouds at 1-m resolution, which means that each point represents 1 m^2 area, resulting in a total of 1.37 million 3D point clouds covering the entire area. This resolution is feasible for accurately representing the actual window positions. First, we marked the window areas based on the 3D imagery from Google Earth and extracted the central points of window areas based on the spatial scale between the images and the collected 3D building footprints. For a few tall windows that required two adjacent points to represent in the vertical direction, such as French windows or glass curtains, only the upper point was maintained to avoid modeling the PVSD twice on the same window in subsequent procedures. Minor adjustments were then made based on site investigation and visual inspection. It shows a satisfactory matching between window areas (Fig. 5a–d) and point clouds (Fig. 5e–h) in the 3D scene.

Hourly solar irradiation data were computed for an entire day with an equal interval of 14 days throughout the year, resulting in a computation of 26 days for the whole year. Each data represents the mean solar distribution over the corresponding 14-day period, which is a suitable trade-off between big-data computation and high temporal resolution. This study developed a Python program to perform the following tasks: (i) aggregating the hourly solar irradiation data by day and thus by month for demonstration purposes; (ii) filtering out the non-building points to avoid unnecessary computation; and (iii) matching the extracted window points denoted by $\mathscr{W}$ to their corresponding positions in the 3D point clouds $\mathscr{P}$. Each window point $w \in \mathscr{W}$ is represented by a unique ID , a 3D coordinate, a building polyline azimuth α, and an interval ν denoting the distance between its upper adjacent window.

3.4. Computation

The solar irradiation estimation model was implemented as a set of hierarchical SQL functions in the database management system PostgreSQL 11 with the support of PostGIS 2.5. Python 3.10 with the support of GeoPandas 0.10.2 were used for the data pre-processing described in Section 3.3, as well as for PVSD modeling and optimization described in Section 2. To cope with the big-data computation, we designed a parallel computational architecture that utilizes six CPU cores to get annual solar distribution through hourly accumulation and run the optimization models.

4. Results

4.1. Spatio-temporal solar potential distribution

The installation of PV modules is preferred in areas where solar irradiation is both numerically high and spatially concentrated. Therefore, it is important to consider the effects of spatio-temporal variations of solar potential distribution over the whole year. In this study, we estimated biweekly solar distribution to represent the mean distribution over the two weeks because seasonal variation is insignificant for this short period in Hong Kong. This allows us to make biweekly solar irradiation accumulation throughout the year based on the spatial index of 3D point clouds. For visual inspection, the equal-interval classification method was used in ArcGIS Pro to create 32 classes based on the same numeric scale and color scheme.

Fig. 6 illustrates the monthly spatial distributions of solar radiation on 3D urban surfaces. The distribution patterns of rooftops and ground are generally similar, with higher irradiation values than building façades. However, shading from surrounding buildings can cause long-term shadowing in some ground areas and lower rooftops and façades, which limits their PV potential. Specifically, the southeast-facing building façades receive more solar irradiation than those facing

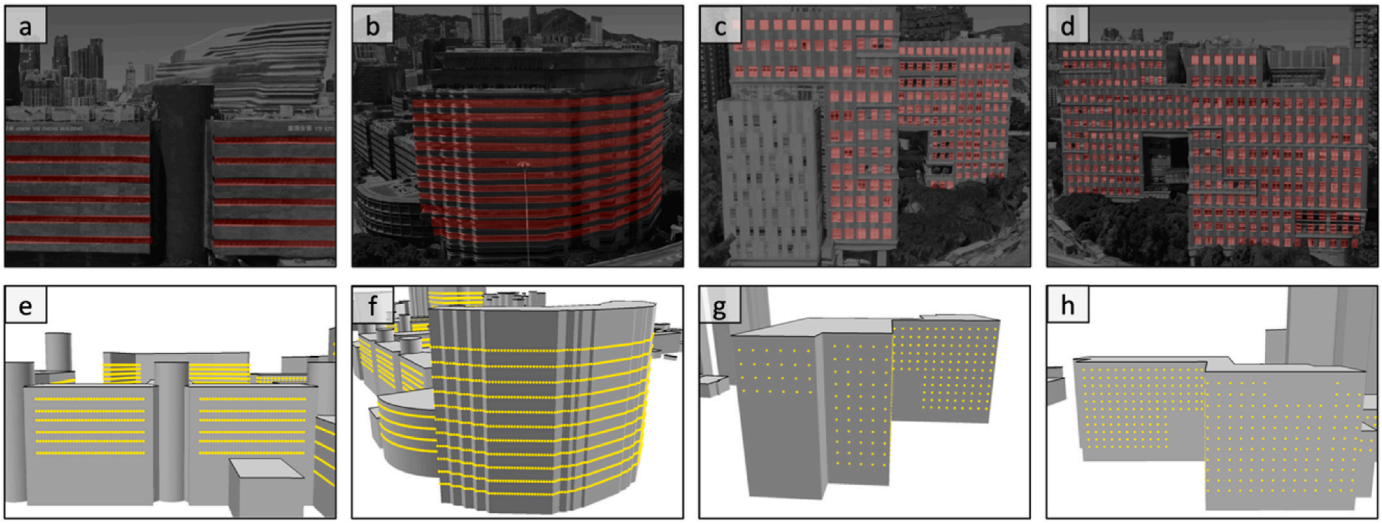

Fig. 5. Visualization of the window areas and the extracted point clouds. (a)–(d) The red rectangles represent the marked window areas. (e)–(h) The yellow points represent the corresponding extracted window points.

southwest, especially during the summer (Fig. 6e–h), when e is very large and β is between [145°, 180°]. On the other hand, the difference of irradiations between southeast- and southwest-facing façades is small during winter (Fig. 6a, k-l). Notably, the weather in Hong Kong was mostly cloudy or partly cloudy in August that created small diffuse proportions, which led to smaller solar potentials compared to July.

4.2. Distribution patterns of solar PV potential

Assuming a conservative and constant system performance ratio of 16.5%, which is the product of a 22% PV module conversion efficiency and a 75% PV system efficiency [48], we derived the PV potential of the PVSD directly from the solar irradiation on the building surfaces. To reveal the temporal variation of power generation for PVSDs on all extracted windows in the three scenarios, the hourly power generation distribution over the twelve months with a 0.5-m-wide PVSD is presented in Fig. 7. The power generation is mainly concentrated between 10:00–12:00 from May to August in SHS (Fig. 7a), and an increased power generation in the morning is observed in SIS, peaking around 10:00–11:00 (Fig. 7b). In contrast, ROS has the highest power generation from 9:00–13:00 in almost all months, and its peak time is around 9:00 from March to September (Fig. 7c). Despite they had different temporal patterns in the morning, all of them experienced a large decrease in power generation since 15:00 all over the year, leading to an inefficient performance in the late afternoon. This is closely related to the varying associations between solar characteristics (i.e., azimuth and elevation angle) and building layouts (i.e., building height, footprint shapes, and orientations). The revealed patterns are essential to optimize PVSDs installations and useful to assess the techno-economic benefits.

However, not all windows are suitable for PVSD installation, and different PV widths may introduce different performances. Therefore, a comparison of the solar PV potential of different scenarios and PV widths with and without threshold is performed and shown in Fig. 8. The threshold TH is set to 60% of the maximum annual electricity generation E_y. Fig. 8a and b illustrate the distribution of E_y before and after applying the threshold, respectively. The boxes represent the lower and upper quartiles, the middle lines represent the median, the whiskers represent 1.5 interquartile range values, the crosses represent the mean, and the dots represent outliers. It is obvious that E_y rises with PV width increases, with ROS producing the most, followed by SIS and SHS. The maximum E_y of a 1-m-long PV module using the ROS reached 354.36 kWh/year, which is 17.53% higher than that using the SIS (301.50 kWh/year), and 57.40% higher than that using the SHS (225.13 kWh/year), reflecting that PVSDs with smaller tilt angle and flexible configuration scenario have vast potential in power generation. Before applying the threshold, the mean E_y of a 1-m-wide PVSD based on the SHS, SIS, and ROS is 73.82 kWh, 95.49 kWh, and 108.45 kWh, respectively, which is 77.25%, 76.31%, and 77.30% higher than PVSDs with the width of 0.5 m, indicating an approximately rising trend of 15% per 0.1-m in all three scenarios. The lower limits for all groups are considerably increased after applying the threshold, and the median values are greater than the mean values.

The mean and median normalized power generation $\widetilde{E}_y$ with and without threshold are calculated for a fairer comparison (Fig. 8c and d). Prior to applying the threshold, the power generation of PVSD per unit area decreases with the PV width increases, and the downward trends are similar among different scenarios. From 0.5m to 1m, the $\widetilde{E}_y$ in ROS is declined from 122.38 kWh to 104.61 kWh. It is mainly because the wider the PVSD, the more shading from upper PVSDs prevents the lower ones from harvesting sunlight. After applying the threshold, a more moderate downward trend is observed, and the absolute gap between mean values of different scenarios widens. When PV width is 0.5 m, the $\widetilde{E}_y$ based on the SHS, SIS, and ROS is 186.10 kWh, 255.29 kWh, and 300.32 kWh, respectively. The results above confirm the benefits of using thresholds to maximize distributed solar farming.

4.3. Optimization of PVSD installation

After identifying areas with high solar potential, the next step is to address the effect of shading. A comparison of effective shading duration τ with threshold is shown in Fig. 9. Given that the E_y alone is not sufficient to determine the optimal PV width, the average effective shading duration throughout the year is used to determine the most appropriate width for each scenario, which will be discussed in details in the following subsections.

4.3.1. SHS-based optimization

From a PV width of 0.5m–0.7m, both the mean and lower bound of τ show a noticeable increase throughout the year under SHS. This implies a significant improvement in the overall shading capacity as the PV width increases. However, the marginal benefit diminishes significantly once the PV width reaches 0.8m and beyond, indicating that increasing the PV width beyond 0.7m has less impact on further enhancing the general shading capacity (Fig. 9a). Hence, the PV width is determined to

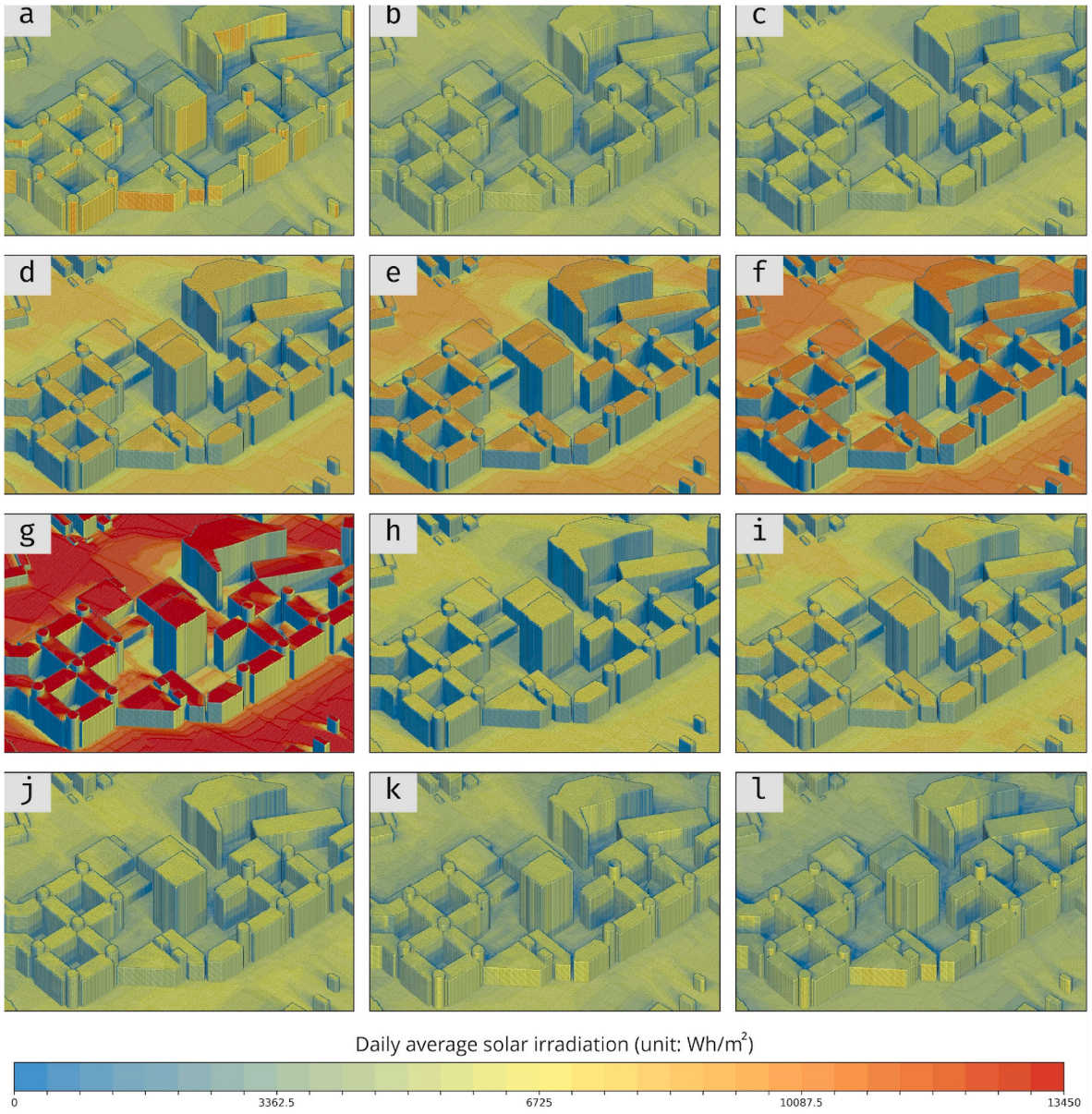

Fig. 6. Daily average solar irradiation on urban surfaces from January (a) to December (l) in 2018.

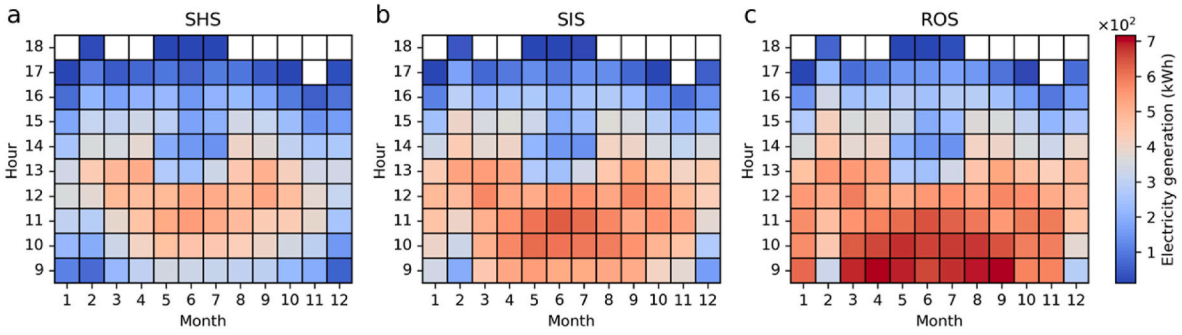

Fig. 7. The electricity generation for all potential 0.5-m-wide PVSDs in the study area under three scenarios varies by month and hour. The white grids represent no data.

be 0.7m in the SHS. Under this configuration, the SHS yields a total of 4737 eligible PVSDs, resulting in a combined E_y of 0.607 GWh. The optimized mean $\widetilde{E}_d$ per unit area per day is 0.501 kWh, and the mean τ is 5.1 h per day, which are 2.3 times and 0.85 times of the unoptimized ones, respectively. As the PV module can only receive a component of solar radiation, the power generation capability of the SHS is the lowest,

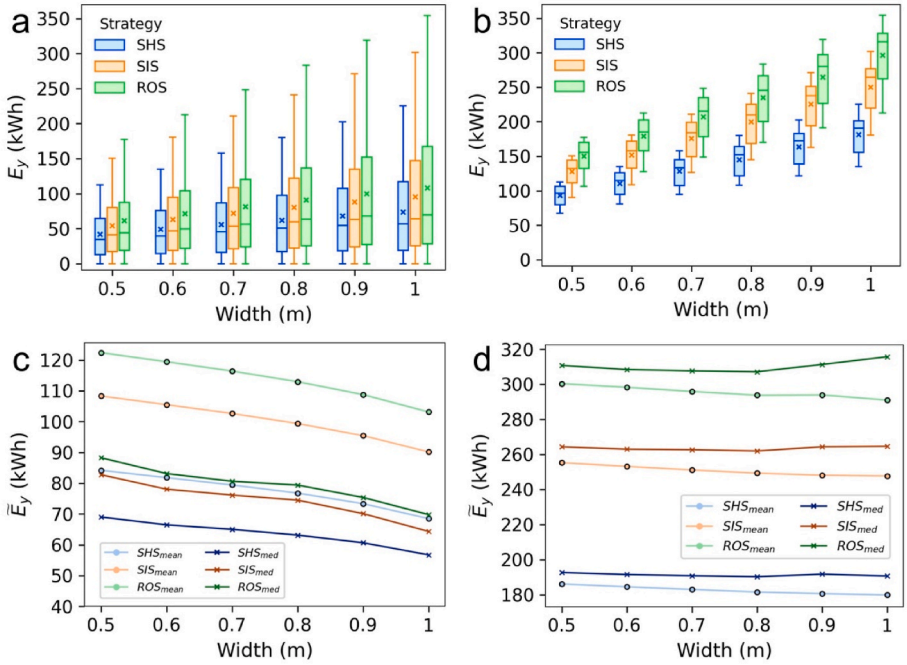

Fig. 8. Comparison of solar PV potential of different scenarios and PV widths with and without threshold. (a) Distribution of E_y without threshold. (b) Distribution of E_y with threshold. (c) Trends of mean and median $\widetilde{E}_y$ without threshold. (d) Trends of mean and median $\widetilde{E}_y$ with threshold.

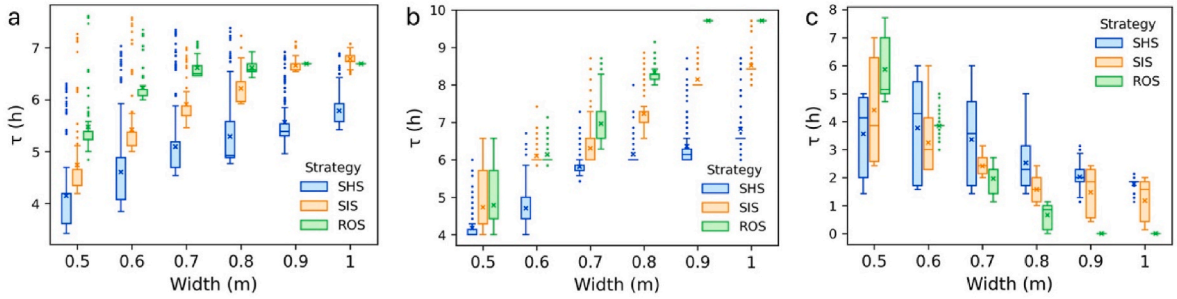

Fig. 9. Comparison of effective shading duration with threshold. (a) The mean shading duration throughout the year. (b) The mean shading duration during summer. (c) The mean shading duration during winter.

with a maximum of about 0.617 kWh/m^2/day. The SHS also has the shortest solar shading duration in summer (Fig. 9b) but has better shading performance in winter (Fig. 9c). Overall, the SHS scenario is only competitive in terms of solar shading in specific seasons in Hong Kong, and can hardly handle year-round power and shading needs.

4.3.2. SIS-based optimization

The SIS strikes a balance between SHS and ROS in terms of power generation and solar shading duration. From a PV width of 0.5m–0.9m, the increment of τ is kept for around 0.48 h. However, from 0.9m to 1.0m, the marginal benefit drops to less than 0.13 h, suggesting that further increasing the PV width does not significantly contribute to additional shading hours. Thus, the PV width is set to 0.9m under the SIS. With this condition, only 18.2% of the PVSDs (4030 units) can yield 46.54% of the total potential power generation (a combined E_y of 0.907 GWh). The mean $\widetilde{E}_d$ is 0.685 kWh/m^2/day, and the mean τ is 6.66 h per day, which are 2.56 times and 0.98 times higher than the unoptimized ones, respectively. One possible limitation is that the effective shading time of some PVSDs may be less than 1 h during winter (Fig. 9c).

4.3.3. ROS-based optimization

The ROS has an adaptive orientation towards solar angles, which has the most solar farming and the most shading of windows and surrounding PVSDs. The box shift dramatically higher along the τ-axis From a PV width of 0.5m–0.7m. However, when going from a PV width of 0.7m–0.8m, the marginal benefit dramatically decreases (Fig. 9a). As a result, the PV width is set to 0.7m in the ROS. In this width, the ROS yields a total of 4159 eligible PVSDs, producing a combined E_y of 0.861 GWh. The mean $\widetilde{E}_d$ is 0.811 kWh/m^2 per day, and the mean τ is 6.61 h per day, which are 2.54 times and 0.96 times than the initial values, respectively. In addition, a width of 0.7m can ensure at least 1 h of effective shading during winter (Fig. 9c) and approximately 7 h during summer (Fig. 9b), without unacceptable shortage in different seasons. This indicates that the ROS successfully provides a balance between shading requirements in various seasons while maximizing solar energy production.

The spatial distribution of the optimized PVSDs is shown in Fig. 10, with a detailed color scheme presented in Table 3. It can be observed that power generation on building façades presents gradual changes, and continuous access to direct solar irradiation can greatly offset the adverse effect of *overshadow* on lower modules across all scenarios. The PVSDs facing southeast have the greatest potential for power generation (Fig. 10a,e,i). For certain south-facing PVSDs within a quadrangle, those with high power potential tend to be concentrated in the central regions

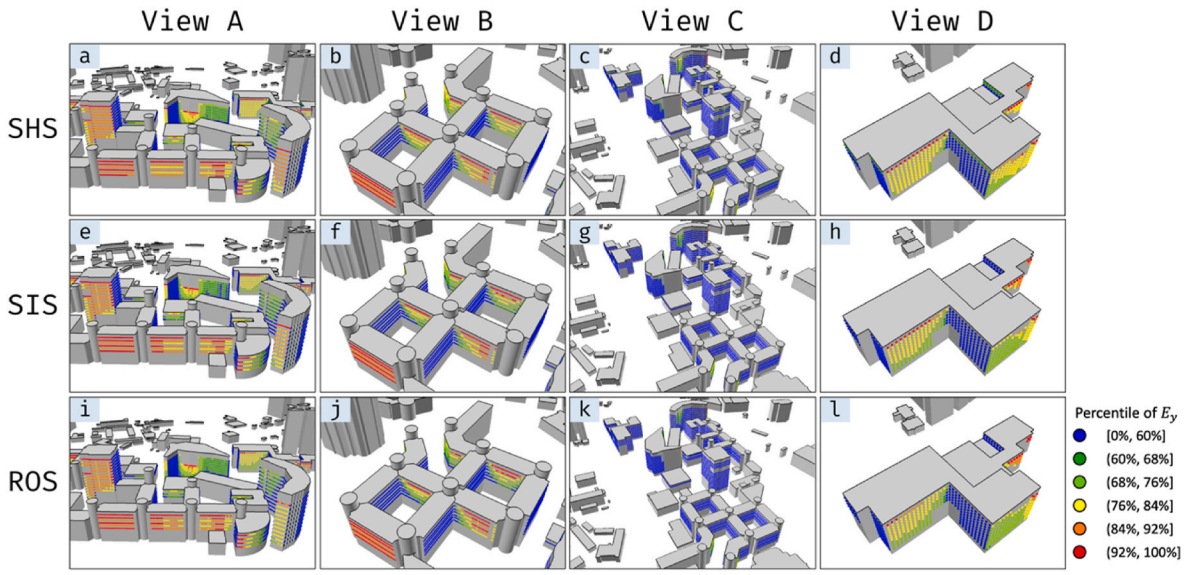

Fig. 10. Spatial distribution of the optimized PVSDs. Panels (a)–(d), (e)–(h), (i)–(l) correspond to SHS, SIS, and ROS, respectively. The characters above each column represent corresponding camera positions shown in Fig. 4, and a detailed color scheme is listed in Table 3.

(Fig. 10b,f,j). While a few PVSDs can be installed on the top floors on the southwestern side under SHS (Fig. 10c), the shaded areas on the same side provide almost no suitable spaces for PVSD installation under SIS and ROS (Fig. 10g,k). The PVSDs in the building shown in View D present a large variation in power potential, with certain areas on the top floor being particularly well-suited for installation (Fig. 10d,h,l).

In summary, given the spatially heterogeneous distribution of solar PV potential, it is essential to consider the economics of PV module deployment. The amount of generated electricity, shading duration, and construction cost all increase as the width of the PVSD increases. It is suggested to concentrate on installing PVSDs on the unobstructed southeastern side and selectively install them on the upper floors of U-shaped buildings that are heavily shaded by neighboring structures. Installing PVSDs every two floors can be considered to minimize the adverse effects of *overshadow*. As for the shady side of the study area, installing PVSDs on the top floor, which is always perpendicular to the wall, might be an appropriate choice.

5. Discussion

Installing PVSDs with a smaller tilt angle can generate more electricity and provide more shade for the indoor environment. Although PVSDs can reduce the need for cooling by regulating the sunlight, there is no need to provide excessive shade indoors. When natural daylight cannot provide the required indoor illuminance, artificial lighting will be switched on, wasting energy. The trade-off between increased electricity production and the potential waste of unnecessary artificial lighting should be carefully considered when designing static inclined shading systems.

Table 3
The detailed color scheme for Fig. 10 under different scenarios.

Symbol	Percentile of E_y	E_y (kWh)		
		SHS (Width: 0.7m)	SIS (Width: 0.9m)	ROS (Width: 0.7m)
●	[0%, 60%]	[0, 93]	[0, 161]	[0, 147]
●	(60%, 68%]	[94, 105]	[162, 189]	[148, 173]
●	(68%, 76%]	[106, 127]	[190, 226]	[174, 208]
●	(76%, 84%]	[128, 143]	[227, 247]	[209, 230]
●	(84%, 92%]	[144, 147]	[248, 253]	[231, 235]
●	(92%, 100%]	[148, 157]	[254, 271]	[236, 248]

PVSDs are cost-effective and can be promoted in urban areas because they not only capture solar energy without taking up additional urban space but also have a positive impact on a sustainable environment by reducing energy consumption for indoor cooling. We suggest that installing PVSDs on building façades only can partially offset the electricity demand of buildings, and systematically integrating rooftop and façade PVs in suitable locations may be a wise solution. In addition, adopting flexible installation scenarios in Hong Kong can help to address the mismatch between supply and actual demand over time and space. For cities around the world with different climates and urban morphologies, it is recommended to choose the installation strategy by comprehensively considering landscape design, installation feasibility, and actual power demand.

The results contain three limitations. Firstly, each point represents an area of 1×1 m^2, and such size may not properly capture the size of certain windows. This means that a few extracted window points may deviate from their actual spatial positions. Thus, the spatial resolution of the 3D point clouds and building footprint can be further improved. Secondly, reflective radiation has not been incorporated into the 3D solar irradiation estimation. This indicates that certain solar accumulative areas created by high albedo surfaces may not have been captured in this study. Nevertheless, this effect should be insignificant as it rarely occurs on façades. Thirdly, using a fixed system performance ratio of 16.5% is a conservative approach. However, it disregards the impact of various factors, including PV module type, tilt angle, temperature, and other environmental conditions. These factors play a crucial role in the real-world power generation process and have the potential to introduce inaccuracy.

Deep learning-based approaches can help resolve some of these issues. For example, using semantic segmentation networks to identify and segment window areas from street view images can provide a cost-effective and consistent method for large-scale data preparation. In addition, utilizing street view images to adaptively classify façades and thus determine their albedos can provide a more comprehensive and accurate estimate for *global* solar irradiation at the city scale [59]. In future large-scale studies, it is also encouraged to carry out actual installations of planned BIPV facilities and compare their performance with the model's estimates. Incorporating error metrics is advantageous for validating the accuracy of the model and identifying potential systematic errors. This approach will contribute to the realization of a more reliable and comprehensive sustainable city.

The study presents a practical, efficient, and transferable solution that enables rapid assessment of the solar PV potential of building components. This approach can be applied to diverse locations characterized by distinctive climates and urban morphologies. The adaptability of the analytical model to new meteorological and geometric datasets, which are readily available for numerous global cities, underscores its versatility. Consequently, this research makes a significant contribution to the development of sustainable cities, and the findings can inspire researchers, urban planners, and investors to promote the development of distributed PV systems in other cities.

6. Conclusion

This study proposes an optimization framework to maximize distributed solar farming and effective solar shading duration while minimizing PV area for PVSDs. A case study in Hong Kong demonstrated the spatiotemporal heterogeneity of solar potential distribution in an urban area, considering real-world weather conditions and shading caused by obstruction. The study modeled the urban surfaces as 3D point clouds, and estimated solar potential on PVSDs with the consideration of shadow effects. Three PVSD planning scenarios are proposed and compared to effectively maximize solar farming and minimize construction costs.

Taking power generation and effective shading duration into account, the PV widths are determined as 0.7m, 0.9m, and 0.7m for SHS, SIS, and ROS, respectively. Remarkably, the ROS outperforms the other two scenarios in terms of both power generation and shading duration. Under the flexible ROS scenario, the optimized 0.7-m-wide PVSDs can generate 0.861 GWh of electricity annually, with a competitive average power generation efficiency of 0.811 kWh/m^2/day and a solar shading duration of 6.61 h/day. The well-suited installation areas for optimized PVSDs are identified from their spatial distribution, and it is suggested to install PVSDs on unobstructed southeast-facing windows and specific top floors. Overall, the estimated PV power generation and solar shading capacity are encouraging and inspiring, which motivates us to promote distributed solar farming using PVSDs.

The precise determination of window positions and building surface reflectance remains a challenge in accurately modeling the power potential of PVSDs within urban environments. Future research can incorporate deep learning-based approaches and conduct real-world installations to validate model estimates and improve the accuracy.

CRediT authorship contribution statement

Yuxuan Ye: Methodology, Software, Data curation, Formal analysis, Visualization, Writing – original draft. **Rui Zhu:** Conceptualization, Methodology, Software, Supervision, Writing – review & editing. **Jinyue Yan:** Conceptualization, Methodology, Writing – review & editing. **Lin Lu:** Conceptualization, Methodology, Writing – review & editing. **Man Sing Wong:** Writing – review & editing, Funding acquisition. **Wei Luo:** Methodology, Writing – review & editing. **Min Chen:** Writing – review & editing. **Fan Zhang:** Writing – review & editing. **Linlin You:** Writing – review & editing. **Yafei Wang:** Writing – review & editing. **Zheng Qin:** Writing – review & editing.

Declaration of competing interest

The authors declare that they have no known competing financial interests or personal relationships that could have appeared to influence the work reported in this paper.

Acknowledgements

Man Sing Wong would like to thank the funding support by the Research Institute for Land and Space (Grant No. 1-CD81), The Hong Kong Polytechnic University; and General Research Fund (Grant No. 15603920 and 15602619), and Collaborative Research Fund (Grant No. C5062-21 GF, C4023-20 GF), from the Hong Kong Research Grants Council, Hong Kong, China.

References

[1] K.C. Seto, S. Dhakal, A. Bigio, H. Blanco, G.C. Delgado, D. Dewar, et al., Human settlements, infrastructure, and spatial planning, in: Climate Change 2014: Mitigation of Climate Change: Contribution of Working Group III to the Fifth Assessment Report of the Intergovernmental Panel on Climate Change, vol. 12, Cambridge University Press, Cambridge, United Kingdom and New York, NY, USA, 2014, p. 927.
[2] P. Pradhan, L. Costa, D. Rybski, W. Lucht, J.P. Kropp, A systematic study of sustainable development goal (SDG) interactions, Earth's Future 5 (2017) 1169–1179, https://doi.org/10.1002/2017EF000632.
[3] J.D. Sachs, G. Schmidt-Traub, M. Mazzucato, D. Messner, N. Nakicenovic, J. Rockstroem, Six transformations to achieve the sustainable development goals, Nat. Sustain. 2 (2019) 805–814, https://doi.org/10.1038/s41893-019-0352-9.
[4] D. Gielen, F. Boshell, D. Saygin, M.D. Bazilian, N. Wagner, R. Gorini, The role of renewable energy in the global energy transformation, Energy Strategy Rev. 24 (2019) 38–50, https://doi.org/10.1016/j.esr.2019.01.006.
[5] K. Saidi, A. Omri, The impact of renewable energy on carbon emissions and economic growth in 15 major renewable energy-consuming countries, Environ. Res. 186 (2020), 109567, https://doi.org/10.1016/j.envres.2020.109567.
[6] S. Chu, A. Majumdar, Opportunities and challenges for a sustainable energy future, Nature 488 (2012) 294–303, https://doi.org/10.1038/nature11475.
[7] R.L. Fares, M.E. Webber, The impacts of storing solar energy in the home to reduce reliance on the utility, Nat. Energy 2 (2017), 17001, https://doi.org/10.1038/nenergy.2017.1.
[8] X. Zhang, S.-K. Lau, S.S.Y. Lau, Y. Zhao, Photovoltaic integrated shading devices (PVSDs): a review, Sol. Energy 170 (2018) 947–968, https://doi.org/10.1016/j.solener.2018.05.067.
[9] J. Han, L. Lu, J. Peng, H. Yang, Performance of ventilated double-sided PV facade compared with conventional clear glass facade, Energy Build. 56 (2013) 204–209, https://doi.org/10.1016/j.enbuild.2012.08.017.
[10] B.K. Koyunbaba, Z. Yilmaz, K. Ulgen, An approach for energy modeling of a building integrated photovoltaic (BIPV) Trombe wall system, Energy Build. 67 (2013) 680–688, https://doi.org/10.1016/j.enbuild.2011.06.031.
[11] K. Bodis, I. Kougias, A. Jager-Waldau, N. Taylor, S. Szabo, A high-resolution geospatial assessment of the rooftop solar photovoltaic potential in the European Union, Renew. Sustain. Energy Rev. 114 (2019), 109309, https://doi.org/10.1016/j.rser.2019.109309.
[12] K. Jeong, T. Hong, C. Ban, C. Koo, H.S. Park, Life cycle economic and environmental assessment for establishing the optimal implementation strategy of rooftop photovoltaic system in military facility, J. Clean. Prod. 104 (2015) 315–327, https://doi.org/10.1016/j.jclepro.2015.05.066.
[13] M.J. Mangiante, P.-Y. Whung, L. Zhou, R. Porter, A. Cepada, E. Campirano, et al., Economic and technical assessment of rooftop solar photovoltaic potential in Brownsville, Texas, U.S.A, Comput. Environ. Urban Syst. 80 (2020), 101450, https://doi.org/10.1016/j.compenvurbsys.2019.101450.
[14] P.K. Ng, N. Mithraratne, H.W. Kua, Energy analysis of semi-transparent BIPV in Singapore buildings, Energy Build. 66 (2013) 274–281, https://doi.org/10.1016/j.enbuild.2013.07.029.
[15] S. Xu, W. Liao, J. Huang, J. Kang, Optimal PV cell coverage ratio for semi-transparent photovoltaics on office building façades in central China, Energy Build. 77 (2014) 130–138, https://doi.org/10.1016/j.enbuild.2014.03.052.
[16] W. Zhang, L. Lu, J. Peng, A. Song, Comparison of the overall energy performance of semi-transparent photovoltaic windows and common energy-efficient windows in Hong Kong, Energy Build. 128 (2016) 511–518, https://doi.org/10.1016/j.enbuild.2016.07.016.
[17] M. Akbari Paydar, Optimum design of building integrated PV module as a movable shading device, Sustain. Cities Soc. 62 (2020), 102368, https://doi.org/10.1016/j.scs.2020.102368.
[18] M. Krarti, Performance of PV integrated dynamic overhangs applied to US homes, Energy 230 (2021), 120843, https://doi.org/10.1016/j.energy.2021.120843.
[19] W. Zhang, L. Lu, J. Peng, Evaluation of potential benefits of solar photovoltaic shadings in Hong Kong, Energy 137 (2017) 1152–1158, https://doi.org/10.1016/j.energy.2017.04.166.
[20] L. Sun, L. Lu, H. Yang, Optimum design of shading-type building-integrated photovoltaic claddings with different surface azimuth angles, Appl. Energy 90 (2012) 233–240, https://doi.org/10.1016/j.apenergy.2011.01.062.
[21] M. Baghoolizadeh, A.A. Nadooshan, S.A.H.H. Dehkordi, M. Rostamzadeh-Renani, R. Rostamzadeh-Renani, M. Afrand, Multi-objective optimization of annual electricity consumption and annual electricity production of a residential building using photovoltaic shadings, Int. J. Energy Res. (2022) 1–41.
[22] J. Peng, D.C. Curcija, L. Lu, S.E. Selkowitz, H. Yang, W. Zhang, Numerical investigation of the energy saving potential of a semi-transparent photovoltaic double-skin facade in a cool-summer Mediterranean climate, Appl. Energy 165 (2016) 345–356, https://doi.org/10.1016/j.apenergy.2015.12.074.
[23] C. Qiu, H. Yang, W. Zhang, Investigation on the energy performance of a novel semi-transparent BIPV system integrated with vacuum glazing, Build. Simulat. 12 (2019) 29–39, https://doi.org/10.1007/s12273-018-0464-6.

[24] M.A. Arnaout, Y.I. Go, A. Saqaff, Pilot study on building-integrated PV: Technical assessment and economic analysis, Int. J. Energy Res. 44 (2020) 9538–9559, https://doi.org/10.1002/er.5204.
[25] M. Panagiotidou, M.C. Brito, K. Hamza, J.J. Jasieniak, J. Zhou, Prospects of photovoltaic rooftops, walls and windows at a city to building scale, Sol. Energy 230 (2021) 675–687, https://doi.org/10.1016/j.solener.2021.10.060.
[26] C. Zomer, I. Custódio, A. Antoniolli, R. Rüther, Performance assessment of partially shaded building-integrated photovoltaic (BIPV) systems in a positive-energy solar energy laboratory building: Architecture perspectives, Sol. Energy 211 (2020) 879–896, https://doi.org/10.1016/j.solener.2020.10.026.
[27] C.L. Cheng, C.S. Sanchez Jimenez, M.-C. Lee, Research of BIPV optimal tilted angle, use of latitude concept for south orientated plans, Renew. Energy 34 (2009) 1644–1650, https://doi.org/10.1016/j.renene.2008.10.025.
[28] M.J. Sorgato, K. Schneider, R. Rüther, Technical and economic evaluation of thin-film CdTe building-integrated photovoltaics (BIPV) replacing façade and rooftop materials in office buildings in a warm and sunny climate, Renew. Energy 118 (2018) 84–98, https://doi.org/10.1016/j.renene.2017.10.091.
[29] G. Lobaccaro, M.M. Lisowska, E. Saretta, P. Bonomo, F. Frontini, A Methodological Analysis Approach to Assess Solar Energy Potential at the Neighborhood Scale, Energies 12 (2019) 3554, https://doi.org/10.3390/en12183554.
[30] H. Gholami, H.N. Røstvik, D. Müller-Eie, Holistic economic analysis of building integrated photovoltaics (BIPV) system: Case studies evaluation, Energy Build. 203 (2019), 109461, https://doi.org/10.1016/j.enbuild.2019.109461.
[31] T. Hong, C. Koo, J. Oh, K. Jeong, Nonlinearity analysis of the shading effect on the technical–economic performance of the building-integrated photovoltaic blind, Appl. Energy 194 (2017) 467–480, https://doi.org/10.1016/j.apenergy.2016.05.027.
[32] M. Mandalaki, S. Papantoniou, T. Tsoutsos, Assessment of energy production from photovoltaic modules integrated in typical shading devices, Sustain. Cities Soc. 10 (2014) 222–231, https://doi.org/10.1016/j.scs.2013.09.001.
[33] M. Mandalaki, T. Tsoutsos, N. Papamanolis, Integrated PV in shading systems for Mediterranean countries: Balance between energy production and visual comfort, Energy Build. 77 (2014) 445–456, https://doi.org/10.1016/j.enbuild.2014.03.046.
[34] B. Weller, C. Hemmerle, S. Jakubetz, S. Unnewehr, Detail Practice: Photovoltaics, Birkhäuser, 2012, https://doi.org/10.11129/detail.9783034615709.
[35] A. Kirimtat, M.F. Tasgetiren, P. Brida, O. Krejcar, Control of PV integrated shading devices in buildings: A review, Build. Environ. 214 (2022), 108961, https://doi.org/10.1016/j.buildenv.2022.108961.
[36] J.E. Ogbeba, E. Hoskara, The Evaluation of Single-Family Detached Housing Units in terms of Integrated Photovoltaic Shading Devices: The Case of Northern Cyprus, Sustainability 11 (2019) 593, https://doi.org/10.3390/su11030593.
[37] L.G. Valladares-Rendón, G. Schmid, S.-L. Lo, Review on energy savings by solar control techniques and optimal building orientation for the strategic placement of façade shading systems, Energy Build. 140 (2017) 458–479, https://doi.org/10.1016/j.enbuild.2016.12.073.
[38] J. Hofierka, J. Kaňuk, Assessment of photovoltaic potential in urban areas using open-source solar radiation tools, Renew. Energy 34 (2009) 2206–2214, https://doi.org/10.1016/j.renene.2009.02.021.
[39] M. Šúri, T.A. Huld, E.D. Dunlop, H.A. Ossenbrink, Potential of solar electricity generation in the European Union member states and candidate countries, Sol. Energy 81 (2007) 1295–1305, https://doi.org/10.1016/j.solener.2006.12.007.
[40] J. Hofierka, M. Zlocha, A New 3-D Solar Radiation Model for 3-D City Models: New 3-D Solar Radiation Model, Trans. GIS 16 (2012) 681–690, https://doi.org/10.1111/j.1467-9671.2012.01337.x.
[41] P. Redweik, C. Catita, M. Brito, Solar energy potential on roofs and facades in an urban landscape, Sol. Energy 97 (2013) 332–341, https://doi.org/10.1016/j.solener.2013.08.036.
[42] C. Catita, P. Redweik, J. Pereira, M.C. Brito, Extending solar potential analysis in buildings to vertical facades, Comput. Geosci. 66 (2014) 1–12, https://doi.org/10.1016/j.cageo.2014.01.002.
[43] M. Bremer, A. Mayr, V. Wichmann, K. Schmidtner, M. Rutzinger, A new multi-scale 3D-GIS-approach for the assessment and dissemination of solar income of digital city models, Comput. Environ. Urban Syst. 57 (2016) 144–154, https://doi.org/10.1016/j.compenvurbsys.2016.02.007.
[44] R. Zhu, L. You, P. Santi, M.S. Wong, C. Ratti, Solar accessibility in developing cities: A case study in Kowloon East, Hong Kong, Sustain. Cities Soc. 51 (2019), 101738, https://doi.org/10.1016/j.scs.2019.101738.
[45] R. Zhu, M.S. Wong, L. You, P. Santi, J. Nichol, H.C. Ho, et al., The effect of urban morphology on the solar capacity of three-dimensional cities, Renew. Energy 153 (2020) 1111–1126, https://doi.org/10.1016/j.renene.2020.02.050.
[46] T. Zhong, K. Zhang, M. Chen, Y. Wang, R. Zhu, Z. Zhang, et al., Assessment of solar photovoltaic potentials on urban noise barriers using street-view imagery, Renew. Energy 168 (2021) 181–194, https://doi.org/10.1016/j.renene.2020.12.044.
[47] R. Zhu, D. Kondor, C. Cheng, X. Zhang, P. Santi, M.S. Wong, et al., Solar photovoltaic generation for charging shared electric scooters, Appl. Energy 313 (2022), 118728, https://doi.org/10.1016/j.apenergy.2022.118728.
[48] R. Zhu, M.S. Wong, M.-P. Kwan, M. Chen, P. Santi, C. Ratti, An economically feasible optimization of photovoltaic provision using real electricity demand: A case study in New York city, Sustain. Cities Soc. 78 (2022), 103614, https://doi.org/10.1016/j.scs.2021.103614.
[49] S. Huang, P.M. Rich, R.L. Crabtree, C.S. Potter, P. Fu, Modeling Monthly Near-Surface Air Temperature from Solar Radiation and Lapse Rate: Application over Complex Terrain in Yellowstone National Park, Phys. Geogr. 29 (2008) 158–178, https://doi.org/10.2747/0272-3646.29.2.158.
[50] R. Zhu, C. Cheng, P. Santi, M. Chen, X. Zhang, M. Mazzarello, et al., Optimization of photovoltaic provision in a three-dimensional city using real-time electricity demand, Appl. Energy 316 (2022), 119042, https://doi.org/10.1016/j.apenergy.2022.119042.
[51] S. Wang, Y.K. Yi, N. Liu, Multi-objective optimization (MOO) for high-rise residential buildings' layout centered on daylight, visual, and outdoor thermal metrics in China, Build. Environ. 205 (2021), 108263, https://doi.org/10.1016/j.buildenv.2021.108263.
[52] A. Nabil, J. Mardaljevic, Useful daylight illuminance: a new paradigm for assessing daylight in buildings, Light. Res. Technol. 37 (2005) 41–57, https://doi.org/10.1191/1365782805li128oa.
[53] Lands Department HKSAR, Hong Kong Geographic Data. https://www.landsd.gov.hk/en/resources/mapping-information/hk-geographic-data.html, 2021. (Accessed 7 October 2022).
[54] EMSD, Hong Kong Energy End-use Data 2021. https://www.emsd.gov.hk/filemanager/en/content_762/HKEEUD2021.pdf, 2021.
[55] K. Lo, Renewable Energy Development in Hong Kong: Potential, Progress, and Barriers, Curr Sustainable Renewable Energy Rep 4 (2017) 50–55, https://doi.org/10.1007/s40518-017-0068-2.
[56] M.S. Wong, R. Zhu, Z. Liu, L. Lu, J. Peng, Z. Tang, et al., Estimation of Hong Kong's solar energy potential using GIS and remote sensing technologies, Renew. Energy 99 (2016) 325–335, https://doi.org/10.1016/j.renene.2016.07.003.
[57] Environmental Bureau HKSAR, Hong Kong's Climate Action Plan 2050. https://www.climateready.gov.hk/files/pdf/CAP2050_booklet_en.pdf, 2021.
[58] World Weather Online, Historical Monthly Weather, 2022. https://www.worldweatheronline.com/. (Accessed 12 October 2022).
[59] F. Xu, M.S. Wong, R. Zhu, J. Heo, G. Shi, Semantic segmentation of urban building surface materials using multi-scale contextual attention network, ISPRS J. Photogrammetry Remote Sens. 202 (2023) 158–168, https://doi.org/10.1016/j.isprsjprs.2023.06.001.